

DIELECTRIC PERMITTIVITY AND DENSITY OF THE SHALLOW MARTIAN SUBSURFACE IN JEZERO CRATER. Titus M. Casademont¹, Svein-Erik Hamran¹, Hans E. F. Amundsen¹, Sigurd Eide¹, Henning Dypvik¹, Tor Berger¹, Patrick Russell² and the Mars 2020 RIMFAX Team, ¹Institute of Technology Systems, Univ. of Oslo, Norway, titus.casademont@its.uio.no, ²Univ. of California, Los Angeles, USA.

Introduction: Perseverance is the first NASA Rover with a ground penetrating radar (GPR) payload, the “Radar Imager for Mars’ Subsurface Experiment” (RIMFAX) [1]. RIMFAX has continuously sounded the upper meter of the Martian subsurface along the Rover traverse in Jezero Crater. First results by Hamran et al. (AGU 2021) include the detection of large scale layering, revealing the geologic succession and possible density flow related origin of the Western Seitah region. Here, we present RIMFAX’ estimates of local radar wave propagation velocity (hereafter ‘velocity’) along the whole rover traverse. From the velocity, the relative dielectric permittivity (‘permittivity’) and bulk rock density (‘density’) are derived. The velocity is crucial to access depth and vertical extension of subsurface features, such as thickness and dipping angle of geologic layers. Both permittivity and density constrain the material type and thus contribute to determining the geologic origin of the subsurface. The permittivities found along Seitah are in good agreement with an igneous rock origin.

Methods:

Hyperbola matching in a two layer setting: A buried diffractor with sub-wavelength radar cross section such as small boulders or cavities scatter the incoming wave incoherently. Hyperbola matching estimates the average overburden velocity above a buried diffractor by fitting the theoretical traveltimes to the corresponding hyperbolic shape in the data. It is a widely used technique in earth based GPR applications and has been used on the Chinese Chang’E 3 and 4 missions as a primary source of velocity determination [2–4]. However, classical hyperbola matching assumes an antenna directly coupled with the ground, which is not the case for rover mounted antennas several 10 cm above ground. In that case, refraction at the air-surface interface with strong refractive contrast has to be taken into account. The geometric rays from antenna to diffractor are no straight lines anymore, and the point of refraction depends on the contrast in refractive indices, governed by Fermat’s principle and Snell’s law. The principle is displayed in Fig. 1 for the two-layer case of free air and a homogeneous subsurface. Waves that get scattered from the diffractor and travel back to the antenna are displayed as rays for certain radiation angles at the diffractor. Fig. 1 inset shows a hyperbolic shape in the data of sol 130, overlain by the hyperbolic curve of Fig. 1. By fitting the analytic curve to the data,

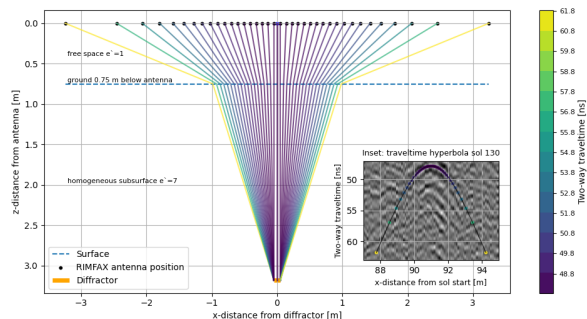


Figure 1: Two layer model with surface refraction and diffractor depth 2.4 m and width 10 cm, ca. $1/6$ of RIMFAX center wavelength. Inset: The ray-geometry and traveltimes for $v = 0.11$ m/ns or $\epsilon' = 7$ fit a hyperbolic shape on sol 130.

the velocity is determined. With v and the center rays the diffractor depth is calculated, which can also represent the out-of-line distance with respect to the rover traverse, due to the 3d wave propagation.

Data processing: Since RIMFAX is a frequency modulated continuous wave radar (FMCW), data processing is centered around a Fourier transform to get the modulated ground reflectivity series [1]. The raw data is corrected by a background removal, before windowing each trace by a Blackman window and zeropadding the front to correct for the radar bandwidth. After Fourier transformation, the RIMFAX gating and loss are compensated for and the starttime corrected to the antenna feedpoint.

From velocity to permittivity and density: For the dry rock and regolith subsurface at Jezero Crater, we assume a non-magnetic, low-loss medium with loss tangent $\tan(\delta) = \epsilon''/\epsilon' \ll 1$ and dielectric loss factor ϵ'' . Then the permittivity is related to the velocity by $v = c/\sqrt{\epsilon'}$. The inversion of permittivity for density is an ongoing field of investigation, with many authors focusing on a Lichtenecker mixing formula approach, resulting in formulas of the form

$$\epsilon' = a^\rho \quad (1)$$

with a constant a varying from 1.85 to 2.22 and density ρ ([5–7] and references therein). However, not all rocks are fitted well by these results, especially the high density and high permittivity igneous rocks measured by [8] and [5]. Fitting the 48 most Martian ana-

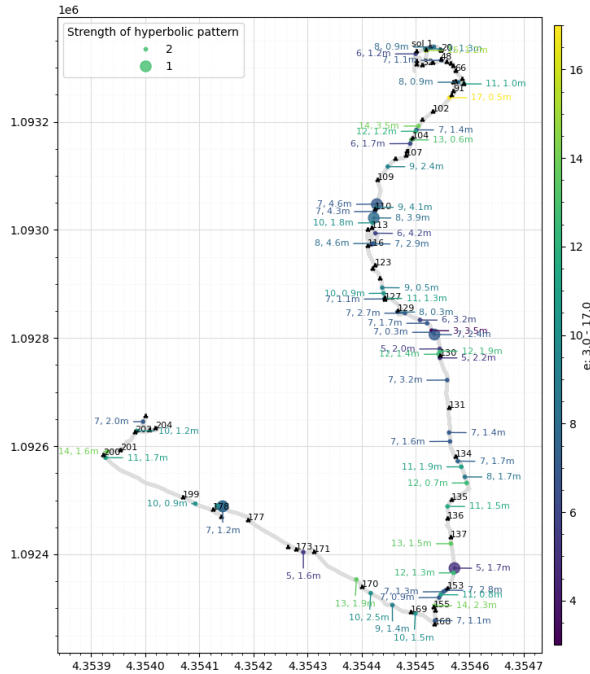


Figure 2: Diffractor distribution along rover traverse until solar conjunction (sol 210), displayed with permittivity of the overburden and depth in *m*. The strongest patterns are marked with bigger dots. Black dots and numbers indicate end of sol locations.

log rocks from [8] with the Lichteneker model, we get $a = 2.48$, implying that the $a = 2$ after [6] might overestimate densities in the realm of high permittivity igneous rocks.

Results and Discussion: Along the rover traverse from landing to solar conjunction (sol 15 to sol 210), we determined 69 hyperbolic shapes in the data. The samples needed to show a symmetric hyperbolic pattern, distinguishable scattered energy and a width large enough to be sensitive to variations in fitting velocity. Even though the data exhibits an abundance of weaker diffractors, the fitting uncertainty for those has been considered to high for velocity determination at this stage. Fig 2 shows the diffractor distribution with permittivities and depth along the rover traverse. Taking the overall permittivity average of the rover path yields $\epsilon' = 9.0 \pm 2.8$ with a mean diffractor depth of $1.9 \pm 1.1m$. The subset of 6 diffractors marked as particularly strong and symmetric yields $\epsilon' = 7.0 \pm 1.1$. Fig. 3 shows the data with the hyperberbolic fits for this subset.

The values point towards a solid rock subsurface with average density $3.2g/cm^3$ for $a = 2$ in Eq. 1 after [6] ($2.4g/cm^3$ for $a = 2.48$). The permittivity and density are typical for igneous rocks that tend to have solid rock

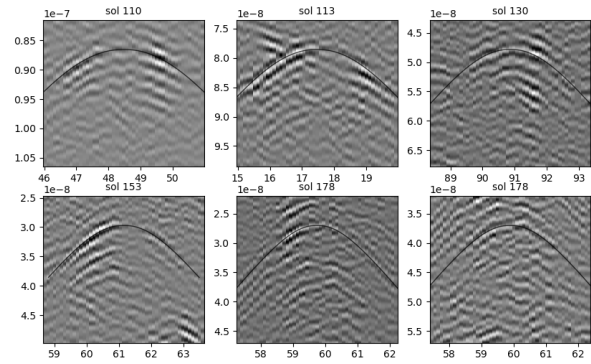


Figure 3: Subset of hyperbolic patterns marked with big dots in Fig. 2. x-axis: distance on sol in *m*, y-axis: two-way travelltime in *s*.

permittivities greater than 6 [9] and frequently reach 20 [8]. They also are in range of lava flow permittivities repeatedly found by SHARAD in the Tharsis region [10, 11]. Notably, this origin is in good agreement with PIXL X-ray Fluorescence measurements on surfacing rocks at the Perseverance drill sites Guillaumes (sol 167) and Bellegarde (sol 187), revealing basaltic lava flows around Seitah [12, 13]. RIMFAX subsurface densities are in range of Supercam’s CIPW derived surface rock densities [14].

Conclusion: The first subsurface permittivity and density estimates by RIMFAX suggest, that large parts of the subsurface along Seitah consists of igneous material. The findings are in good agreement with PIXL’s results on the abraded patches. Further work will be needed to quantify hyperbolic matching ambiguities, emphasize weak diffractors in processing, develop permittivity-density inversion in high permittivity igneous regimes and apply advanced raytracing for complex subsurface geometries.

[1] Hamran S.-E. et al. (2020) *Space Sci. Rev.*, 216(8). [2] Jol H. M., *Ground Penetrating Radar (GPR) Principles*, ELSEVIER (2009). [3] Lai J. et al. (2016) *Planet. Space Sci.*, 120. [4] Li C. et al. (2020) *Sci. Adv.*, 6(9). [5] Rust A. et al. (1999) *J. Volcanol. Geotherm. Res.*, 91(1). [6] Ulaby F. T. and Long D. G., *Microwave radar and radiometric remote sensing*, Univ. of Michigan Press (2014). [7] Hickson D. et al. (2018) *Icarus*, 306. [8] Shmulevich S. A. et al. (1971) *Earth Physics*, (12). [9] Campbell M. J. and Ulrichs J. (1969) *J. Geophys. Res.*, 74(25). [10] Carter L. M. et al. (2009) *Geophys. Res. Lett.*, 36(23). [11] Simon M. N. et al. (2014) *J. Geophys. Res.: Planets*, 119(11). [12] Schmidt M. E. et al. (2022) *LPSC*. [13] Kizovski T. V. et al. (2022) *LPSC*. [14] Wiens R. C. et al. (2022) *LPSC*.